Research Works for Risk Assessment Technology Related to Flood in Urban Area

Tomotsuka TAKAYAMA, Kaoru TAKARA, Keiich TODA, Masaharu FUJITA,
Hajime MASE, Yasuto TACHIKAWA, Nozomu YONEYAMA,
Daizo TSUTSUMI, Tomohiro YASUDA and Takahiro SAYAMA

Synopsis

The present paper describes research works which have been obtained from the following research topics in our COE research project on the risk assessment technology of flood in urban area and its practical application: 1) 3-D numerical analysis for inundation process of small underground space in urban flood, 2) stability analysis of a shelter tower at exertion of tsunami, 3) porosity of sediment mixtures with different type of grain size distribution, and 4) flood prediction system for highly regulated river basin and its extension to real-time flood forecasting system.

Keywords: numerical analysis, inundation process, small underground space, urban flood, VOF method, tsunami shelter tower, tsunami force, drag coefficient, tsunami velocity on land, porosity of sediment mixtures, grain size distribution, flood prediction system, highly regulated river basin, real-time flood forecasting system

1. Introduction

The research on the risk assessment technology of flood in urban area and its practical application has been performed by the Fluvial and Coastal Research Division as a part of the 21st Century COE Research Project. This paper briefly describes the results of the research activities performed by the Division in the Japanese fiscal year of 2006. The research activities in the paper are classified into four research topics: 1) 3-D numerical analysis for inundation process of small underground space in urban flood, 2) stability analysis of a shelter tower at exertion of tsunami, 3) porosity of sediment mixtures with different type of grain size distribution, and 4) flood prediction system for highly regulated river basin and its extension to real-time flood forecasting system.

2. 3-D Numerical Analysis for Inundation Process of Small Underground Space in Urban Flood

2.1 Background

In the central districts of large cities, under ground space facilities have been developed. During floods, the flow would extend to the under ground space and the damages incurred would be serious.

The inundation process occurring in large-scale under ground spaces, such as an underground mall and a subway, has been studied (Toda *et al.*, 2003; Sekine and Kawakami, 2005). However, the processes occurring in the small-scale underground spaces such as basements of small buildings and small residences have not been sufficiently examined. The floor space and volume of small underground spaces are smaller than those of large underground spaces. If inundation water intrudes into a small underground space, the inundation height would rapidly increase, causing the serious accidents in the underground space. Therefore, it is imperative to study the inundation flow behavior in small underground spaces from the viewpoint of disaster prevention.

Yamamoto *et al.* (2006) carried out an inundation experiment for small underground spaces and showed that it became difficult to take refuge because of a sudden increase in the water depth in a short time. They applied the pond model ~ used for flood analysis ~ and an inundation analysis to an underground inundation experiment. They showed that the model can approximately simulate the time variations in the water depth and that it cannot exactly simulate the initial process occurring during inundation. This study suggests that it is important to accurately predict the initial process occurring at the time of the inundation in order to facilitate evacuation from small underground spaces.

On the other hand, the indexes obtained from refuges in underground spaces, such as the evacuation limit through a flat area (Kamei, 1984) and the evacuation limit through a staircase and door (Ishigaki *et al.*, 2005), have been suggested. Because the main parameter of these indexes is the water depth, an examination of the evacuation possibility requires the accurate prediction of the water depth. In the underground spaces in an urban area, the basement floor is not flat and the staircases are complicated shape. Therefore, numerical methods that can simulate a three-dimensional fluid flow are required for a careful examination of the evacuation possibility. Therefore, in this study, a three-dimensional numerical analysis model with the VOF method is applied to a small underground space including the stairs and the validity of this model is verified.

2.2 Numerical analysis model

In this study, we have developed a numerical analysis model (VOF model) based on a three-dimensional incompressible fluid analysis method. The free surface behavior is analyzed with the VOF method using this model. In this paper, our numerical analysis model referred to as the VOF model.

Water deformation is analyzed by using the VOF method. In this method, the surface shape is expressed with F value (volume occupation rate of each computation cell). The variation of F is calculated by using the following advection equation:

$$\frac{\partial F}{\partial t} + u_j \frac{\partial F}{\partial x_j} = 0 \qquad (2.1)$$

In our model, some schemes are used to exactly satisfy the mass conservation law (Yoneyama and

Moriya, 1995; Yoneyama, 1998). Computation cells are classified into fluid cells, surface cells, and air cells according to their F values. If $0<F<1$, the cell is classified as a surface cell. However, in our study, in order to restrict the extremely rapid spread of the inundation area, the cell adjacent to the floor surface is classified as the air cell up to a water depth of 1mm.

2.3 Application to the flow over a staircase
(1) Real-sized staircase model test

Fig. 2.1 shows a real-scale inundation staircase model. In this test, the velocity and water depth were measured at the bottom of the staircase under the condition that the water depth on the top of the staircase, H, is constant. The measurement section is shown in Fig. 2.1. The value of H is increased from 10cm to 50cm in 10cm intervals. Velocities at nine points in the measurement section are measured by using a Pitot tube.

(2) Comparison of the computed and experiment results

The three-dimensional numerical analysis model with the VOF method (VOF model) is applied to the fluid flow in the model test, where the computation mesh precisely reproduces the shape of the model.

The computation region is shown in Fig. 2.1. Figure 2.2 shows the vertical section of the computation mesh. With regard to the mesh divisions, the tread length (0.2m) and height (0.15m) of the stairs were divided in half and the width of stair was divided into ten equal meshes. The total number of cells was 110,864.

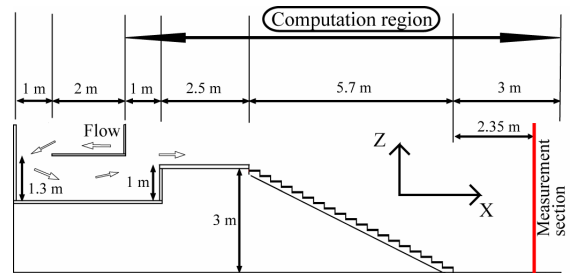Fig. 2.3 shows the section-averaged velocity at the
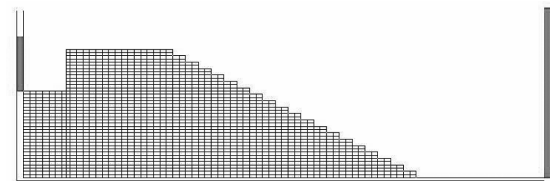

Fig. 2.1 Real-sized staircase model
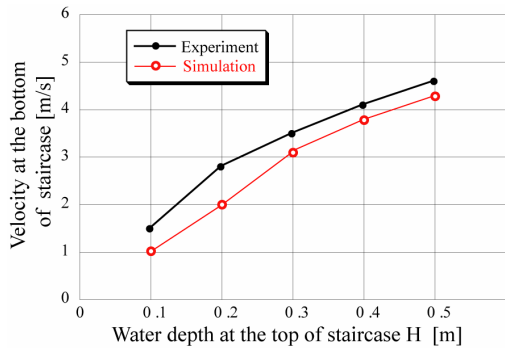

Fig. 2.2 Computation mesh (vertical section)

Fig. 2.3 Comparison of the velocity at the bottom of the staircase
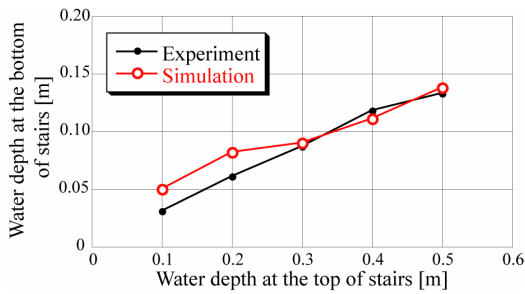

Fig. 2.4 Comparison of the water depth at the bottom of the staircase
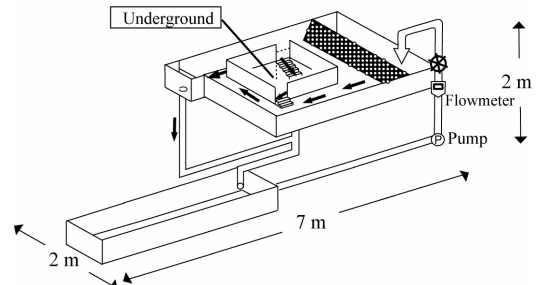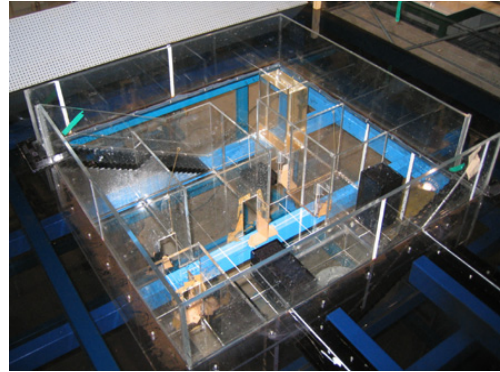

Fig. 2.5 Small underground space model

Photo 2.1 Basement floor of the small underground space model

Fig. 2.6 Basement floor of the small underground space model

bottom of the staircase, and Fig. 2.4 shows the water depths in the same section. In these figures, the computed results are compared with the experiment results.

As shown in Fig. 2.3, the computed values for velocity are slightly less than the experimental values. In this computation, the fluid flow is calculated by using only two mesh divisions because the water depth at the measurement section is less than the height of a single stair (0.15m), which implies that the mesh division is too large to exactly simulate a complex fluid flow at the bottom of the staircase. For this reason, the difference in the results is within an allowable range. On the other hand, the computed water depth approximately agrees with the experimental values. Consequently, we decided that the VOF model is applicable to the fluid flow over a staircase.

2.4 Application to the small underground space model

(1) Small underground space model test

The underground space model is a 1/15 scale hydraulic model of the basement of a conventional small scale building comprising two stairs, hallway, and five rooms. The model can simulate the inundation water behavior that flows toward the basement through the staircases from the ground level and spreads in this region.

Fig. 2.5 shows the small underground space model. Photo 2.1 shows the basement floor of the small underground space model. Fig. 2.6 shows a plane view of the basement floor and measurement points of the inundation depth.

In the experiment, the entrances to the basement are

Table 2.1 Experimental conditions

	Intrusion staircase	Water depth at the ground level	Door state	Removable wall
Case1	A	0.033 m	Open	No
Case2	A	0.033 m	Open	Yes

closed at first and water flows toward the ground level of the model. Here, the water depth is maintained constant by an overflow weir. The entrances are opened up at the start of the model test, and water flows into the basement.

Time variations of the inundation depths in the basement are measured by an ultrasonic water level sensor. The measurement points are shown in Fig. 2.6. The inundation process occurring in the basement is recorded by a digital video camera. The experimental conditions are listed in Table 2.1.

(2) Numerical analysis method

Our VOF model is applied to the fluid flow in the model test, where the computation mesh precisely reproduces the shape of the model. The computation region is the basement section of the hydraulic model. Fig. 2.7 shows the computation mesh. The computation mesh comprises rectangular cells that are adapted to the steps of the stairs, thickness of the wall, and the shapes of objects in the basement. With regard to the mesh divisions, the tread length (2cm) and height (1cm) of a stair were divided in half and the width of a stair was divided into ten equal meshes. The number of cells was 616,896.

The inundation flow enters from the upper part of stairs under the condition that water depth at the ground level, H, is always 0.033m. According to the experiments of Yamamoto *et al.*(2006), the flow rate is $9.1 \times 10^{-4} \text{m}^3/s$ when H=0.033m. The time step Δt=0.001s. In this study, our model is compared with the pond model proposed by Yamamoto *et al.* Fig. 2.8 shows the pond divisions in the pond model. The basement floor is divided in 30 ponds. In their simulation, the inundation flow is introduced into the pond (pond number = 30) located at the bottom of the staircase because they were unable to simulate the fluid flow over staircases.

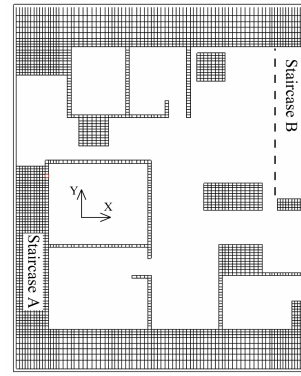**(3) Comparison of the computated and experiment results**

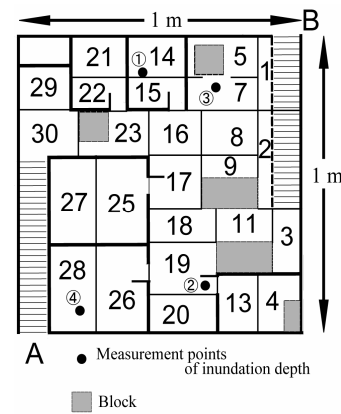Fig. 2.7 Computation meshes for the real-size staircase model

Fig. 2.8 Pond divisions and pond numbers model

Fig. 2.9(a)~(d) show the time variations in the inundation depth at measurement points No.2 and No.4. In these figures, the experiment data and the computed data using the VOF model and the pond model are shown. Fig. 2.10 shows the inundation process computed by using the VOF and pond models. In the figure, the inundation fronts as observed in the experiment are shown.

The time variations in the inundation depth at point No.2 for both the VOF and pond models are in good agreement, as shown in Fig. 2.9(a) and (c). As shown in Fig. 2.9(b), the arrival times of the inundation at point No. 4 for both the models are in good agreement with the experimental data. However, the inundation depth for the pond model increases faster than those for the experiment and VOF model.

To investigate for this reason, a comparison of the time variations in both the models is shown in Fig. 2.9(d). In the VOF model, the water depth at the bottom of the staircase is greater than 5cm when the computation time is 14 s. However, at the same point in time, the water depth in pond number 30 is 2~3cm.

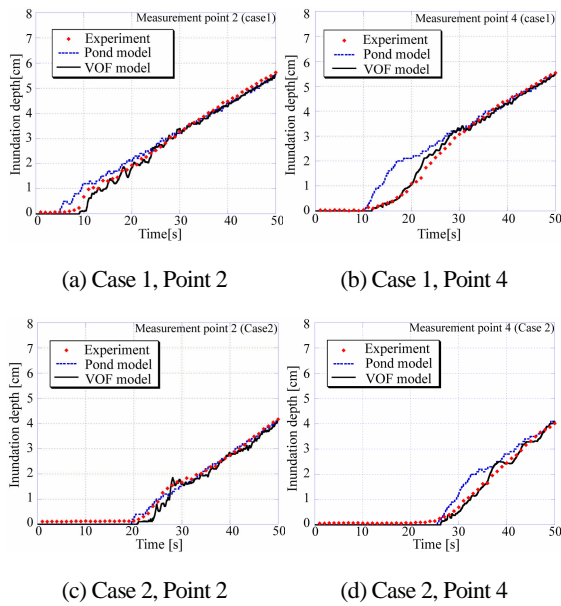In the pond model, it is difficult to simulate the fluid

(a) Case 1, Point 2   (b) Case 1, Point 4

(c) Case 2, Point 2   (d) Case 2, Point 4

Fig. 2.9 Comparison of the time variations in the inundation depth

Fig. 2.10 Comparison of the time variations in the inundation behavior

Fig. 2.11 Studied areas for the evacuation possibility and the state of the doors

flow along the direction of increases in the water depth, because the main driving factor is a difference in the water depths. Therefore, the spread of the inundated area is appropriately simulated, but the partially swollen surface where water accumulated could not be simulated. As a result, in the pond model, inundation water that is not accumulated spreads faster and the inundation depth at point No.4 increases faster than those in the experiment and VOF model. On the other hand, the difference in the water depths between the pond model and the experiment at point No.4 for Case 2 is smaller than that of Case 1, as shown in Fig. 2.9(d). This is because the inundation water accumulates near the bottom of staircase A with the removable wall.

The VOF model can appropriately simulate the spreading of the inundation area, as shown in Fig. 2.10. The pond model can effectively simulate the behavior of inundation front. However, as shown in Fig. 2.10 (T=3~4 s), it cannot simulate the inundation flow flowing straight and spreading behind staircase B.

2.5 Evacuation possibility examination

In this section, we examine the evacuation possibility from an underground space by means of our VOF model. The water depths at the four areas shown in Fig. 2.11 are examined by using our VOF model.

The inundation conditions are as follows. Water flows in from both staircases A and B. The water depth at the ground level, H, rises from 0 to 25cm in 43 s and H
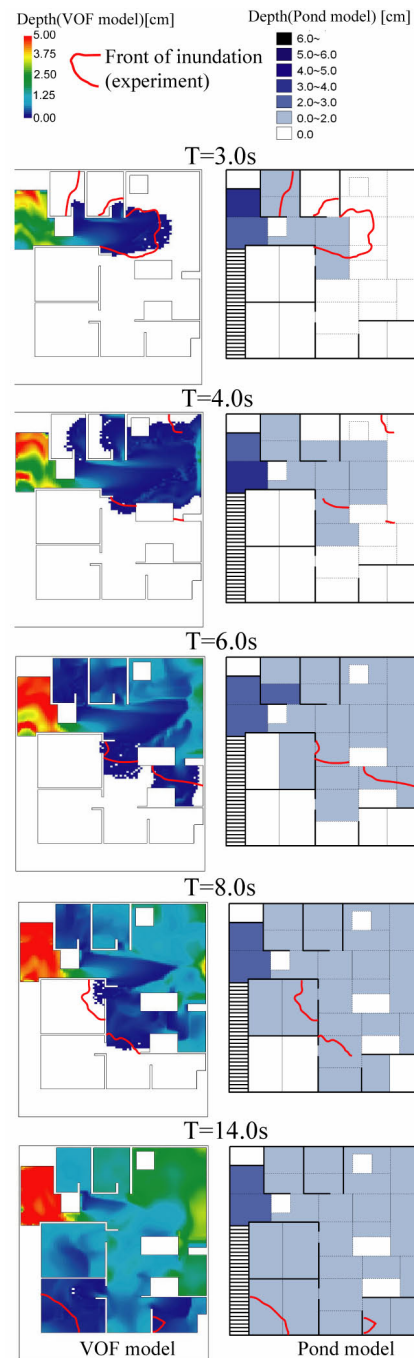
is constant thereafter. Doors A, C and E are open, and the other doors are closed.

Fig. 2.12 shows water surface configuration at a computation time of 77.5 s.

Fig. 2.13 shows the time variation in the inundation depths in the four examined area. The indexes obtained from the refuges in the underground space, such as the evacuation limit through a flat area and the evacuation limit through a staircase and door are shown in the figure. The evacuation limits through a flat area, as suggested by Kamei (1984), are a water depth of 0.70m for adult males, 0.50m for adult females, and 0.30m for children. The evacuation limit through staircases, as suggested by Ishigaki *et al.* (2005), is that the water depth at the ground level, *H*, is 0.3m. The evacuation limit through a door, as suggested by Ishigaki *et al.*, is a water depth of 0.4m at the front of the door. The evacuation possibility can be easily examined by comparing the water depths computed with there indexes.

By using Fig. 2.13, the evacuation possibilities of the inundation conditions can be illustrated as follows. It is difficult for children to evacuate through a flat area (Area 1) after 43 s from the start of inundation. It is difficult to evacuate through door C after 107 s and difficult to evacuate through door E after 116 s. It is difficult for an adult male to evacuate through all the flat areas after approximately 116 s.

2.6 Section's conclusions

The main conclusions of this section can be summarized as follows.

- The three-dimensional numerical analysis model with the VOF method (VOF model) can efficiently simulate the inundation process in small underground spaces.
- The pond model can appropriately simulate them, too: but there are some situations where the configurations of the water surface cannot be simulated.
- The VOF model can be easily used to examine the evacuation possibility by comparing the computed water depths with the indexes obtained from the refuges in underground spaces.

In this study, the simple underground space model is used on the basis of the verification performed by a numerical analysis. We will apply the present numerical analysis model to the multilevel underground space including complex staircases.
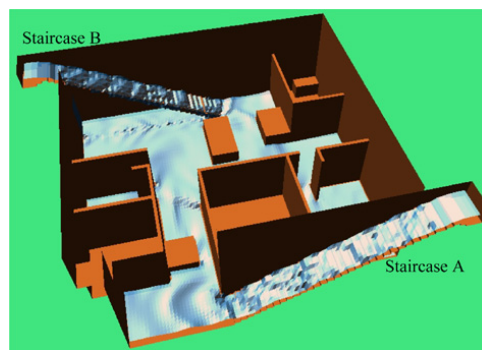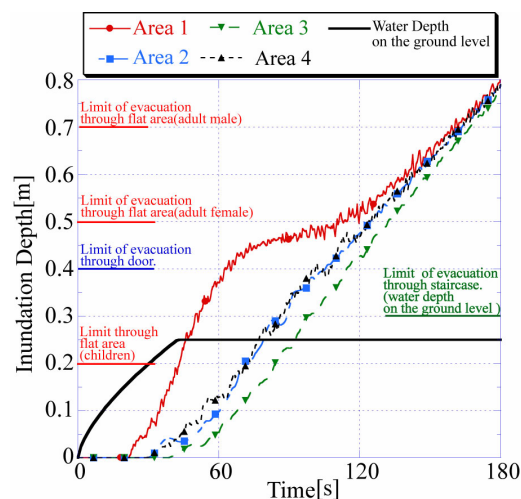

Fig. 2.12 Water surface at 77.5s

Fig. 2.13 Time variation of the studied area and limits of the water depths for safe evacuation

3. Stability Analysis of a Shelter Tower at Exertion of Tsunami

3.1 Background

The occurrence possibility of Tokai, Tonankai and Nankai earthquakes in next 30 years is predicted as more than 50%. These earthquakes will generate great tsunamis, which will attack the Pacific Coasts of Shikoku, Kinki and Tokai. The tsunami will arrive at the coasts within ten minutes after the shaking, and the height of tsunami will reach 5m or more. Residents in these affected areas can do nothing but climbing up to the hill to escape from the tsunami since the high building made of reinforced concrete is few. To save their lives from the tsunami, a shelter tower is designed and started to be constructed by the local governments. Total weight of the tower is 16t, and the column is made of steel pipes of 0.4m in diameter. The evacuation deck is at 5.8m high, and the capacity of the shelter is about 80 refugees. In this study, the hydraulic experiment is performed to check the stability of the tsunami shelter.

3.2 Experimental setup

The tower model (model scale: 1/25) was installed on the measurement plate, and the total force due to the tsunami action on the shelter was measured by the load cell which was installed into the base plate as shown in Photo 3.1. Tsunami was generated as a solitary wave of which amplitude is 5.0m in prototype. The wave gauge and propeller type velocity meter were installed in front of the tower. When tsunami runs up on land, a lot of debris will be carried shoreward by the tsunami. If the debris stack and block up the space between the columns, the tsunami force on the tower may be increased. Therefore, we changed position and permeability of plates which assumed as the debris set between the columns as shown in Fig. 3.1.

3.3 Characteristics of tsunami force acting on shelter

(1) Effect of aperture ratio of assumed debris plate

Fig. 3.2 shows the tsunami force against the aperture ratio of assumed debris plate. In the case of tower position Case T4 with impermeable debris plate, the force was largest F=4.45kgf (43.6N). The force of Case T2 became about three quarter of Case T4. For the cases of T2 and T4 the tsunami force decreases almost linearly against the increasing of aperture ratio. On the other hand, for the Case T3 there is little effect by the aperture ratio of the debris plates.

(2) Stability of shelter tower

In the case of tower itself (Case T1), the tower is enough stable because the tsunami force is smaller than the shear strength of the column connections. On the other hand, if the force is increased by debris, overturning moment becomes much larger than the resistant moment by the tower weight without considering the pullout resistance force of the columns.

(3) Drag coefficient

Drag coefficient can be estimated from Eq.(3.1) (Cengel and Cimbala, 2006).

$$F = \tfrac{1}{2}\rho A(1-\varepsilon)C_D u^2 \tag{3.1}$$

where F is the drag force, C_D is the drag coefficient, ρ is the mass density of fluid, A is the frontal area, ε is the aperture ratio of the plate and u is the flood velocity.

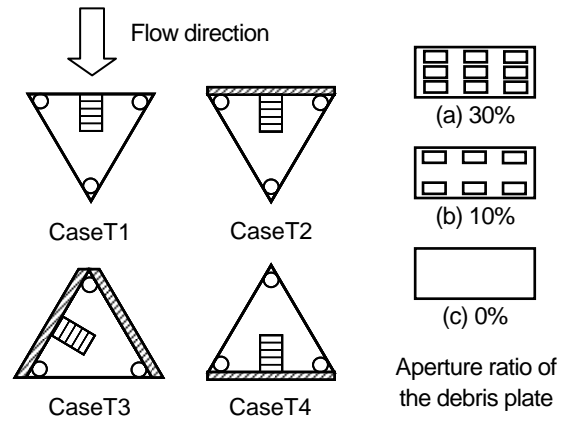Fig. 3.3 shows the drag coefficient against the

Fig. 3.1 Experimental condition (shaded area indicates the assumed debris plate)
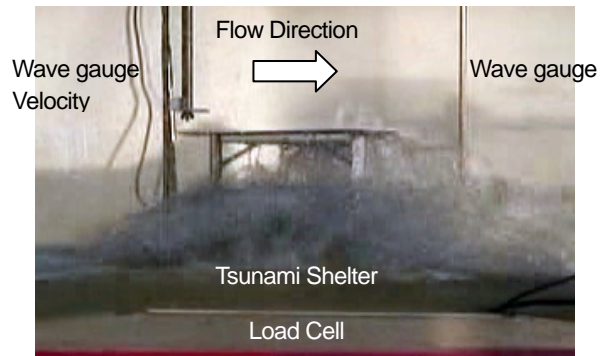

Photo 3.1 Snapshot of exertion of the tsunami against the shelter (CaseT4, Aperture ratio of the debris plate ε=10%)

aperture ratio of the assumed debris plate. There were no typical difference between the Case T1 and Case T2, C_D was about 0.6. On the other hand, for the Case T4, it increases and became 0.8.

(4) Tsunami velocity on the ground

The relationship between the tsunami velocity on the ground, u, and the crest height, η, is obtained by Matsutomi and Izuka(1998) as follows:

$$u = 2\sqrt{g\eta} \tag{3.2}$$

This equation is obtained as the envelope of the field measurement data; sometimes the value becomes too large. Thus, we decided to reexamine the method of presuming the flow velocity of the runup tsunami. The flow velocity of the tsunami is generally represented by the following equation:

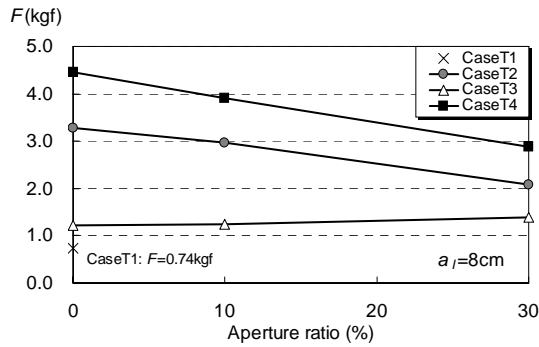$$u = \eta\sqrt{g/(h+\eta)} \tag{3.3}$$

Fig. 3.2 Tsunami force against the aperture ratio of the assumed debris plate
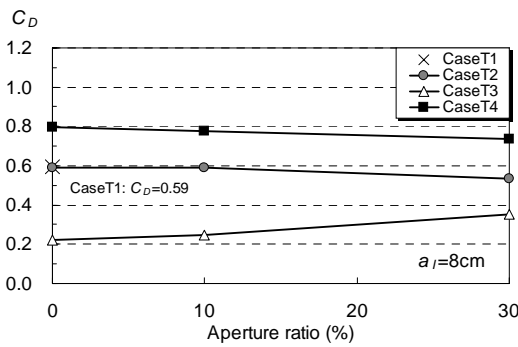

Fig. 3.3 Drag coefficient against the aperture ratio of the assumed debris plate

Flow velocity can be expressed by the next equation by using the relation on the damping of tsunami height which is the flow velocity of the tsunami becomes 0 at the position of maximum runup height R.

$$u = \alpha \sqrt{g(R - h_G)} \qquad (3.4)$$

where h_G is the ground level where the structure is set up.

The coefficient α was examined by using the empirical formula of the maximum tsunami runup height by Togashi *et al.* (1977) and Yasuda *et al.* (2006). It became 1.1 and 0.8 respectively and $\alpha = 0.95 \approx 1$ was obtained as the averaged value. By using the tsunami velocity on the ground estimated from Eq.(3.4) and the drag coefficient obtained from the experiments, presuming of the tsunami force which acted on the land structure such as the tsunami shelter became possible.

3.4 Section's conclusions

The hydraulic experiment was performed to check the stability of tsunami shelters against tsunamis' attack.

It was confirmed that if there are no debris, tower is enough stable since the tsunami force is smaller than the shear strength of the column connections. On the other hand, if the force is increased by debris, overturning moment becomes much larger than the resistant moment by the tower weight without considering the pullout resistance force of the columns. Presuming of tsunami force which acted on land structures such as the tsunami shelter was proposed by using newly derived tsunami velocity equation and the drag coefficient of the structures.

4. Porosity of Sediment Mixtures with Different Type of Grain Size Distribution

4.1 Background

Among the qualitative features of bed material, the grain size distribution and the porosity are very important properties governing a habitat condition of aquatic living things. Particularly, many ecologists are interested in the void structure of the bed material. The previous bed variation models are available for the analysis of bed variation and the change of grain size distribution. However, they cannot provide any result on the change of the porosity. They are, therefore, incomplete for assessing the qualitative change of bed material from an ecological point of view. Fujita *et al.* (2005) have presented a framework of riverbed variation model to simulate the change of porosity as well as bed variation. The porosity is connected with the grain size distribution in their model. In this study, a method for classifying the grain size distribution and a method for obtaining the porosity for each distribution are discussed.

4.2 Classification

(1) Data

Riverbed materials have a variety of different characteristic size, but the grain size distribution could be classified into some types. One of the most typical density functions of grain size is a log-normal distribution. The grain size distribution of bed material in most sand-bed streams is unimodal and that in many gravel-bed rivers is bimodal (Parker, 2004). Also in mountainous rivers, the surface bed material has usually Talbot distribution of grain size (Tatsuzawa *et al.*, 1998).

The grain size distribution of natural riverbed material and produced sediment were collected for analysis of classification and identification of grain size

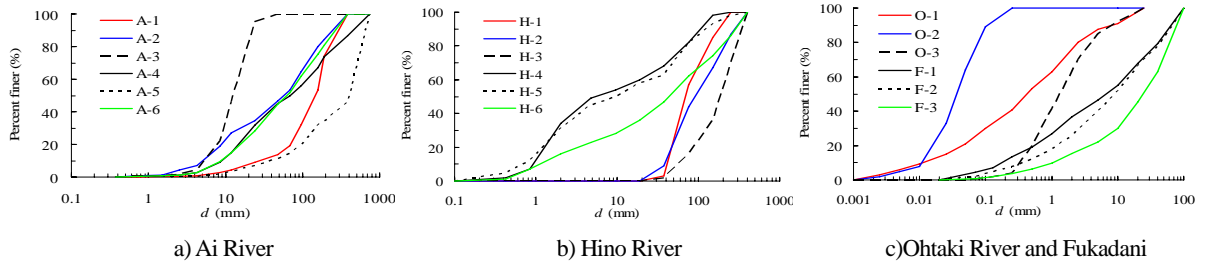| a) Ai River | b) Hino River | c)Ohtaki River and Fukadani |

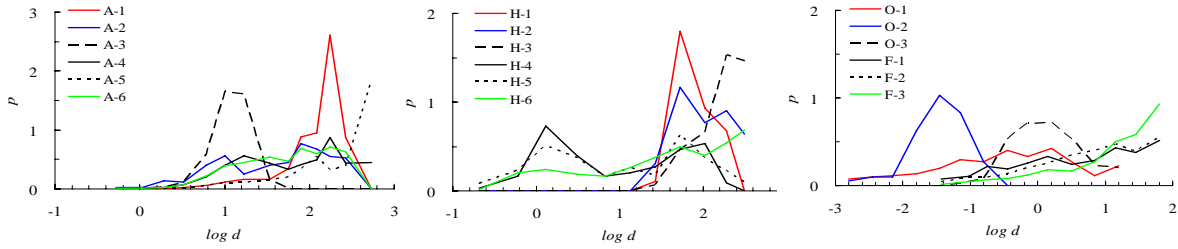Fig. 4.1 Grain size distributions of bed material and produced sediment

Fig. 4.2 Density distributions of grain size distribution shown in Fig. 4.1

distribution. The samples were taken from Ai River (Fujita, 2004), Hino River (Hinogawa River Office of MLIT, 2004), Ohtaki River (Ashida *et al.*, 1987) and Fukadani bare slope. The grain size distributions f and those density functions p are shown in Figs. 4.1 and 4.2. Capital letter A, H, O and F denote the samples from Ai River, Hino River, Ohtaki River and a Fukadani bare slope, respectively. The samples were classified by the characteristics of sampling points as follows:

(a) Surface bed material (A-1, 5, H-1, 2, 3)
(b) Sub-surface bed material (A-2, 6, H-4, 5, 6)
(c) Sand bar (A-3)
(d) Sediment deposition in a sabo dam (A-4)
(e) Sediment deposition in a valley immediately after Ontake Landslide 1984 (O-1)
(f) Sediment deposition in a reservoir (O-2, 3)
(g) Sediment produced at a bare slope (F-1, 2, 3)

(2) Typical grain size distribution

The grain size distributions shown in Fig. 4.1 are roughly classified into three types of grain size distribution, namely, log-normal distribution, Talbot distribution and bimodal distribution. Typical of the grain size distributions of sediment mixture are shown in Fig. 4.3, where *f* is the percentage of the finer grain size and p (= df/d(log$d$)) is the density function of grain size.

(a) Log-normal distribution

Log-normal grain size distribution is shown in Fig. 4.3(a). The density function is as follows:

$$p(\ln d) = \frac{1}{\sqrt{2\pi}\sigma_L} \exp\left[-\frac{(\ln d - \ln d_{mg})^2}{2(\sigma_L)^2} \right] \qquad (4.1)$$

where d_{mg} = the geometric average of grain size and σ_L = standard deviation of ln$d$. Normalizing d with d_{mg}, σ_L is only a parameter of the log-normal distribution. The porosity of the mixture is, therefore, dependent on σ_L.

(b) Talbot distribution

It is well known that the surface bed material of mountainous rivers has Talbot type of grain size distribution shown in Fig. 4.3(b). The grain size distribution function is as follows:

$$f(d) = \left(\frac{d}{d_{max}} \right)^n \qquad (4.2)$$

where d_{max} is the maximum grain size and n is a coefficient. The actual Talbot distributions were fitted with Eq.(4.2). The result shows that a narrow distribution can be expressed by Eq.(4.2), but the difference is much larger for the finer size of the wide distribution. This result indicates the minimum grain size as well as the maximum size should be introduced into the distribution as a parameter. Therefore, Eq.(4.3) is defined as a similar distribution with Talbot distribution. The porosity of the mixture is determined with Talbot number, n_T ($n_T > 1$),
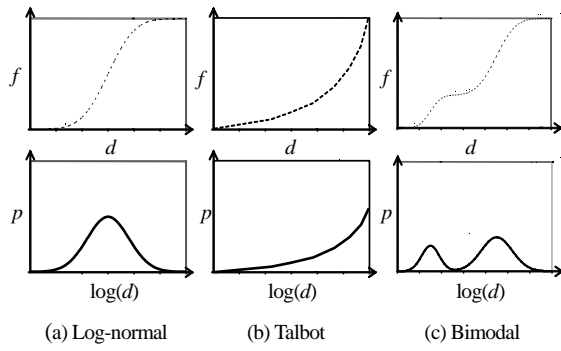
(a) Log-normal   (b) Talbot   (c) Bimodal

Fig.4.3 Typical of grain size distribution of sediment mixture
and the density function of grain size

Fig.4.4 Relation between β and γ

and d_{max}/d_{min}.

$$f(d) = \left(\frac{\log d - \log d_{min}}{\log d_{max} - \log d_{min}} \right)^{n_T} \quad n_T > 1 \qquad (4.3)$$

(c) Bimodal distribution

A grain size distribution is said to be bimodal if the density distribution $p(d)$, displays two distinct peaks. Each peak is a mode of a portion of the distribution. The grain size distribution shown in Fig. 4.3(c) is the bimodal distribution composed of two log-normal distributions with different mean size and standard deviation. When the geometric averages of grain size are d_{mgA} and d_{mgB}, the standard deviation are σ_{LA} and σ_{LB}, the mixing ratio are p_A and $p_B (=1-p_A)$, the parameters governing porosity are σ_{LA}, σ_{LB}, d_{mgA}/d_{mgB} and p_A.

(3) Identification and classification

The grain size distributions of natural sediment mixture can be identified and classified visually based on the shape of size distribution and density distribution. The grain size distribution classified into log-normal distribution if the trend of the size distribution curves similar to log-normal curve and the density distribution has a single peak. If the density distribution is skewed towards a high-end tail of distribution, the grain size distribution is classified into Talbot distribution. If the density distribution has two peaks, the grain size distribution classified into bimodal distribution.

As shown in Fig. 4.3, the shapes of density function p are quite different from each other. Therefore, the type of grain size distribution can be identified if an index expressing the shape of density function p found out. Figure 4.3 shows the number of peak of density function
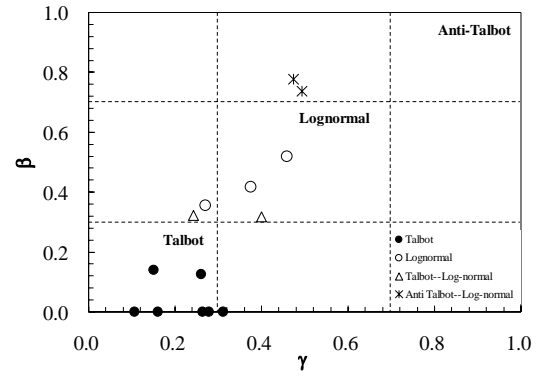
for bimodal distribution is two. It is easy to understand that the number of peak, n_p, is an index for determine of unimodal or bimodal. A-2, A-4, H-4 and H-5 are therefore, identified as bimodal distribution.

In addition, the following two indices are taken:

$$\beta = \frac{\log d_{max} - \log d_{peak}}{\log d_{max} - \log d_{min}}, \quad \gamma = \frac{\log d_{max} - \log d_{50}}{\log d_{max} - \log d_{min}} \quad (4.4)$$

where d_{min} is minimum size, d_{50} is 50% size, d_{max} is maximum size, and d_{peak} is a diameter which give maximum value of p. These indices designate the relative locations of d_{50} and d_{peak} between d_{min} and d_{max}. β and γ are 0.5 for log-normal distribution and 0.0 for Talbot distribution. Actually, the critical value of these indices should be determined for each type.

A type of the distribution can be determined by the shape of size distribution, the shape of density distribution, and values of β and γ. Figure 4.4 shows the relation between β and γ. A-1, A-5, A-6, H-6, F-1, F-2 and F-3 plotted with filled circles are visually identified as Talbot distribution. H-3 and O-1 plotted with triangles are visually identified the distribution between Talbot and log-normal. A-3, O-2, O-3 plotted with open circles are visually identified as log-normal distribution. H-1 and H-2 plotted with cross are the distribution between log-normal and Anti-Talbot. Anti-Talbot distribution is defined by Eq. (4.3) with value of Talbot number, n_T, less than 1 ($n_T < 1$).

Based on the visual identification and the relation between β and γ, the critical value of these indices for each type distribution can be determined. The critical values of the indices were determined by adding and reducing the value of β and γ for log-normal distribution with certain value α. According to the relation between β and γ as shown in Fig. 4.4, the value of (=(0.2 is

reasonable. Grain size distributions are classified into Talbot type if β (0.3 and γ (0.3, log-normal type if $0.3<\beta<0.7$ and $0.3<\gamma<0.7$ and Anti-Talbot type if >0.7 and $\gamma>0.7$.

4.3 Relationship between grain size distribution and porosity

Tsutsumi *et al.* (2006) have developed a particle-packing model generating the porosity of a sediment mixture. The validity of the model was assessed with a laboratory experiment, in which six different-sized spherical glass beads were prepared and mixed well to form six different kinds of particle size distribution. The model results showed that the porosity is associated with the grain size distribution.

(1) Log-normal distribution

Porosity whose grain size distribution of the materials is log-normal distribution with a standard deviation of 0 to 1.5 was calculated by means of the packing model. A relationship between the standard deviation σ_L and the calculated porosity is shown in Fig. 4.5. If the standard deviation σ_L is between 0.01 and 0.1, the porosity is about 0.38. This value is close to the value (0.4) generally used in conventional calculations on riverbed variation. The porosity decreases to 0.156 when the standard deviation σ_L increases to 1.50. When the particle size is widely distributed, the porosity takes much smaller value than 0.4. The porosity increased drastically from 0.33 to 0.38 when the standard deviation σ_L increase slightly from 0.0 to 0.1. This means that the porosity increases drastically if particles with a different size are put into a uniform material.

(2) Talbot distribution

Porosity of the material whose grain size distribution is Talbot distribution with the varies value of Talbot number, n_T, was calculated by means of the packing model. Ratios of maximum and minimum size (dmax/dmin) are 10 and 100. A relationship between the value of Talbot number, n_T, and the calculated porosity is shown in Fig. 4.6. The porosity increased from 0.241 to 0.314 for $d_{max}/d_{min}=10$ when the Talbot number, n_T, increased from 2 to 8. The porosity increased from 0.173 to 0.273 for $d_{max}/d_{min}=100$ when the Talbot number, n_T, increased from 4 to 12. Smaller ratio of d_{max}/d_{min} gives the higher value of porosity.
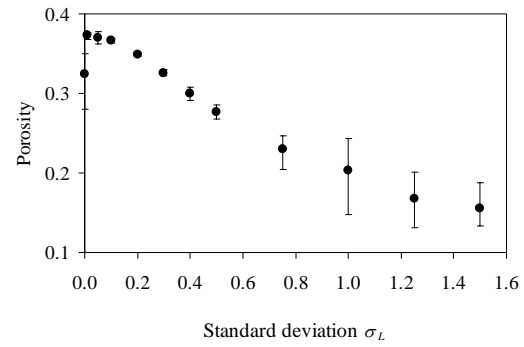

Fig. 4.5 Relationship between the standard deviation, σ_L, and the porosity
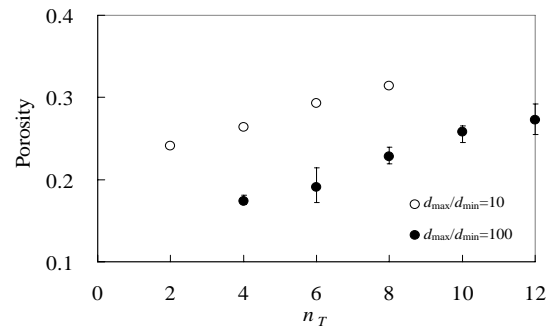

Fig. 4.6 Relationship between the Talbot number, n_T, and the porosity

(3) Bimodal distribution

Generally, bimodal distribution ranges widely. A simulation of its porosity by means of packing model needs much time. Considering the simulation time, in this study the artificial bimodal distributions with narrow distribution were used. The characteristic of materials are shown in Table 4.1. Porosities for seven different fine proportions p_A (i.e., 0, 0.2, 0.25, 0.3, 0.5, 0.75 and 1) were estimated. Relationship between fine proportion p_A (by volume) of mixture and the porosity for two fraction mixtures are shown in Fig. 4.7. The porosity of two component mixtures depends on the fractional concentrations of each particle size population. The results were compared with the porosity of two-particle mixture presented by Fujita (2005). Interestingly, the change of porosity for two particles mixture and two fractions mixture is similar and a porosity minimum is observed.

4.4 Application

The presented method and results in the previous section are applied to estimate the porosity of actual riverbed material. Three different types of actual grain size distribution that represent the log-normal distribution

Table 4.1 Characteristic of sediment for bimodal distribution

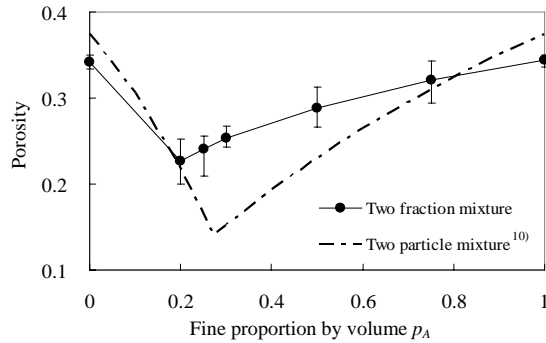| Fraction	σ	d_{min} (mm)	d_{50} (mm)	d_{max} (mm)
A	0.2	0.5	1.0	2.0
B	0.2	2.0	4.0	8.0

Fig. 4.7 Relationship between the fine proportion of mixture and the porosity

(A-3 and H-1) and Talbot distribution (A-5) were selected. The standard deviation for A-3 and H-1 were determined from the data of grain size distribution. Talbot number for A-5 was determined by means of fitting curve defines by Eq.(4.3). Then, the porosity of each grain size distribution was determined by using the diagram of relationship between the geometric parameter of grain size distribution and the porosity. The porosities obtained from the diagram were compared with the porosity estimated by using packing model.

The standard deviation of A-3 and H-1 obtained from the data are 0.60 and 0.52. Talbot number of A-5 is 4. The porosity of A-3, H-1 and A-5 obtained from the diagram are 0.25, 0.27 and 0.19 respectively. The porosity of A-3, H-1 and A-5 obtained from packing model simulation are 0.23, 0.29 and 0.22 respectively. The discrepancy of porosity for lognormal distribution may be due to the distribution of actual grain sizes are not symmetric, while the assumption using a log-normal type of equation is that the grain size distribution is symmetric. In the case of Talbot distribution, the discrepancy of porosity may be due to the grain size distribution was dominated by large particles.

4.5 Section's Conclusions

A method for obtaining the porosity for different types of grain size distribution was developed. The results are as follows:

(1) Grain size distribution of actual sediment mixture can be roughly classified into three types of distribution, namely, log-normal distribution, Talbot distribution and bimodal distribution, based on the mode of density distribution and indices β and γ. However, to determine the exact distribution type, we need to find out another index.

(2) Relationship between the grain size distribution and the porosity can be determined by using the geometric properties of grain size distribution. The porosity of log-normal distributions decreased with an increasing standard deviation. The porosity of Talbot distributions increased with an increasing of the Talbot number n_T and smaller ratio of d_{max}/d_{min} gives the higher value of porosity. The porosity of bimodal distribution depends on the percentage of each fraction in the mixture. In case of the mixture of two fractions under the condition, the minimum porosity was found if the percentage of finer fraction is 0.20.

(3) The porosity could be reasonably estimated by means of the presented method and it could be introduced into the bed variation model.

Although the simulation method was assessed by the laboratory experiment with the glass beads, however, it is not known whether these results represent the void properties of natural riverbed materials. Further assessment of the method with the porosity of natural riverbed materials is required.

5. Flood Prediction System for Highly Regulated River Basin and Its Extension to Real-time Flood Forecasting System

5.1 Background

The alterations of hydrological cycle caused by environmental change indicate that observed information with past or current conditions may not be applicable for future predictions. It is essential for risk assessment of flood to understand the scientific background of hydrological alterations induced by human activity and to predict the future hydrological cycle based on the understandings. One of the crucial flow regime changes is caused by dam reservoirs.

We have focused on flood control with multi-purpose dams, which are operated in a complicated manner based on dam operation rules. The developed dam model in this study predicts outflow and water level with the input information of inflow, upstream rainfall and cooperative
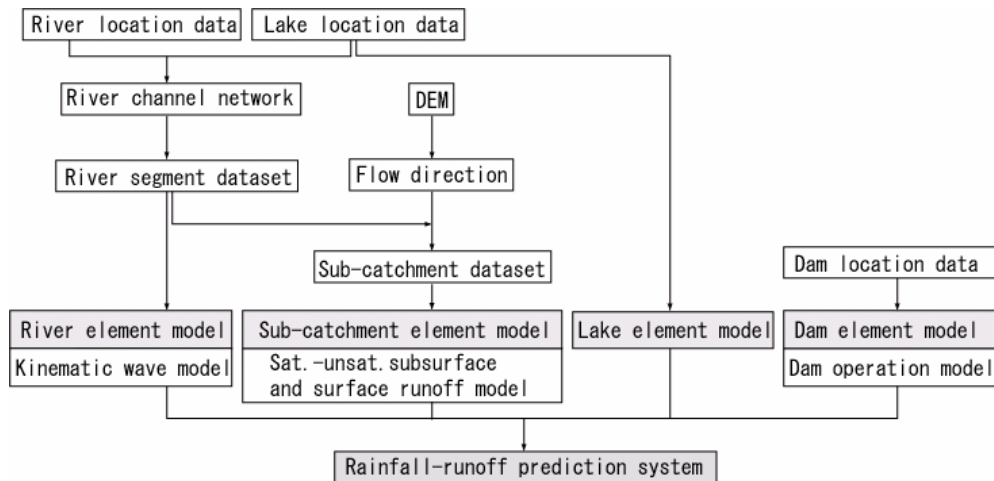
Fig. 5.1 Data processes and the whole structure of the system

dam operations by modeling dam operation rules. A hydrological prediction system is constructed by incorporating the dam models with a distributed rainfall–runoff model. We developed this system for a highly regulated Japanese river basin, the Yodo River basin (7281km^2). By using the developed system, we assess dam effects on flood control to investigate how the flood safety level has been increased by newly constructed dams and to understand which range of flood magnitudes the dams can regulate effectively. Moreover, the system is extended to a real-time river discharge prediction system integrated with a short-term rainfall prediction system.

5.2 A distributed rainfall-runoff prediction system incorporating dam operation model (Sayama, 2005)

(1) Structure of the rainfall-runoff prediction system

The rainfall–runoff prediction system is constructed based on "Object-oriented Hydrological Modeling System (OHyMoS)". The following four kinds of element models compose the whole system (Fig. 5.1).

(a) River element model: The kinematic wave model is applied to a river segment, which is prepared from the digital river-network data and the location information of lakeshores. Each river segment is cut to be about 3 km length.

(b) Sub-catchment element model: A saturated - unsaturated subsurface and surface runoff model (Tachikawa *et al.*, 2004) is applied to all grid-cells composing a sub-catchment. We used a digital elevation model with 250 m resolution to calculate the flow direction and to define the sub-catchment of each river

segment.

(c) Lake element model: Lake element model is a simple mass-balance model to simulate water level from inflow, outflow, and rainfall information. We apply this model to Lake Biwa, of which outflow is simulated with the dam element model.

(d) Dam element model: A dam operation model is constructed with if-then style based on each dam operation rule. We apply it to eight multi purpose dams in the basin. We refer this site-specific dam operation model as a dam element model.

(2) Dam element model

By formulating the dam operation rules and decision-making processes of dam operators, we develop the dam operation model. It predicts the outflow and water level of a dam with the input information of inflow, average rainfall in the dam catchment, and operation status of other related dams.

All the dams located in the Yodo River basin are multi-purpose dams. Although each dam has different operating rules, we can categorize all the flood control operations into the following six common operation processes (Ichikawa, 2001): Ordinary operation; Operation under flood warning; Preliminary release operation; Peak attenuation operation; Flood release operation; and Post flood operation.

Each dam is always under one of the six operations, and we formulate the conditions to shift from one operation to another with if-then equations. Fig. 5.2 (left) shows how to shift the process from one to another, and Fig. 5.2 (right) shows specific water levels that appear in the dam operation rules.
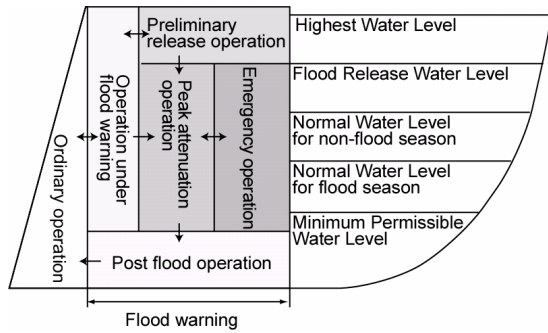
Fig.5.2 Operation statuses and specific water levels of dam operation model

Fig. 5.3 Yodo River basin (7281 km^2)

5.3 Application to the Yodo River basin

(1) Study area

The Yodo River basin is analyzed in this case study because it is a typical Japanese river basin highly regulated by multi-purpose dams. The total area of the Yodo River basin is 8240 km^2. In this case study, since Hirakata is the main design target location for designing dams and other river works, we focus on the upper Hirakata basin (7281km^2) (Fig. 5.3), and refer to this basin as the Yodo River basin in this paper.

There are eight multi-purpose dams inside the basin and five of these dams are located in one of the sub-basins, called the Kizu River basin (1596km^2). The Setagawa weir controls outflow from Lake Biwa (670 km^2), which is the largest Lake in Japan. The mean annual precipitation of the Yodo River basin is about 1600mm.

We conducted a test simulation using observed rainfall and observed discharge data during a typhoon event in 1997. The period of the simulation is from 25 July to 29 July. We used the nearest neighbourhood method to distribute rainfall data that is observed by 58 raingauge stations inside the basin. The estimated total rainfall over the basin is 149mm.

We divide the whole basin into three zones depending on the land use, and assign different parameters in the different land use zones. There are three land use categories: forest, paddy field, and urban area, among which forest is the dominant land-use (63%). A rainfall–runoff model considering surface flow is used for the paddy field zone and the urban area zone. Six dams and Biwa Lake are also simulated in the rainfall–runoff simulation system. Two dams constructed after 1997 are not included in this simulation.
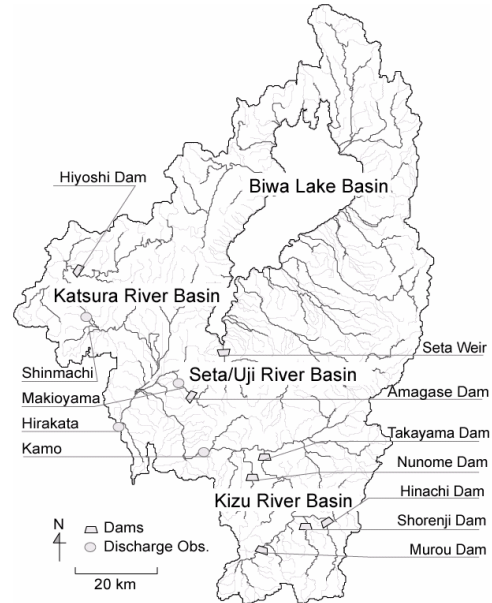
(2) Simulation results

Figure 5.4 shows the simulated and observed inflow and outflow at the Shorenji dam. The good agreement between the simulated inflow with the observed inflow verifies the rainfall–runoff model at the upstream of the dam. The outflow from the dam operation model shows that the preliminary release and peak attenuation operations were properly simulated. Figure 5.5 shows the simulated and observed water level at the Shorenji dam. It shows that the water level is drawn down by the preliminary release and it is increased by the peak attenuation operation.

Figure 5.6 shows the simulated and observed discharge at Kamo. The simulation result excluding the dam element models is also displayed in the figure. By comparing simulated hydrographs with and without dams, it was concluded that the dams located upstream of Kamo could attenuate the peak flood by around 1300 m^3/s.

5.4 Analysis of dam effects on flood control

Construction of large-scale dams is believed to have improved the safety level of a catchment against flood disasters. However, it is not clear to what extent these dams have improved the safety level or which range of flood magnitudes dams can regulate efficiently. In terms of the Yodo River basin, there are currently eight large-scale dams in the basin and seven dams were constructed after 1960. Conducting rainfall–runoff simulation using the developed rainfall–runoff prediction
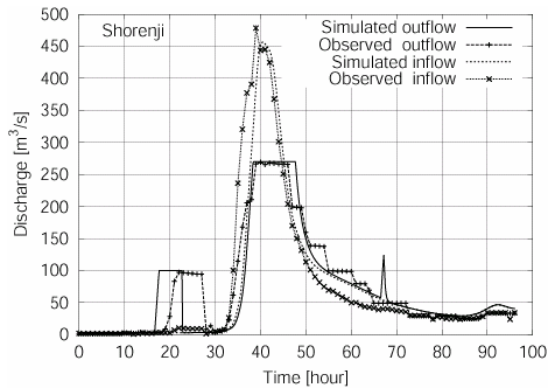
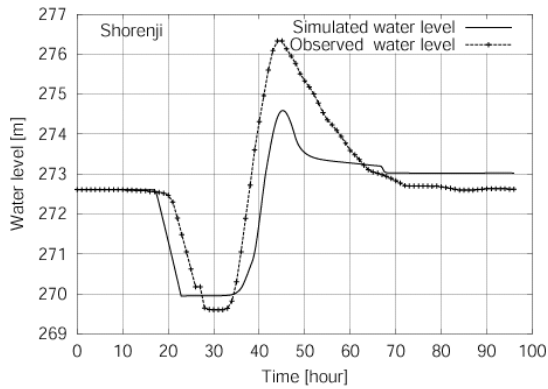Fig. 5.4 Simulated and observed inflow and outflow at Shorenji dam

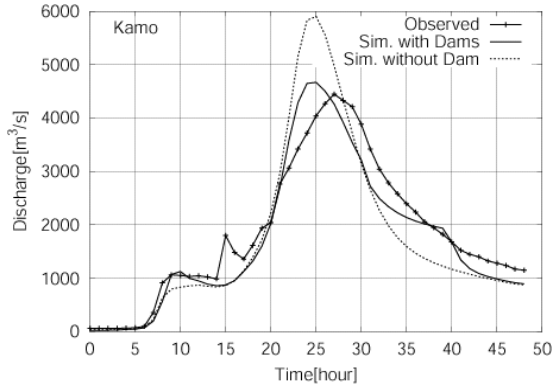Fig. 5.5 Simulated and observed water level at Shorenji dam

Fig. 5.6 Simulated discharge (with and without dams) and observed discharge at Kamo

system, we evaluate how the flood safety level of the Yodo River basin has been progressively increased over the period 1960 to 2000 with respect to rainfall events of different magnitude.

(1) Methods

Rainfall-runoff simulations were implemented considering the dams that were operated at the beginning of the following years: 1960, 1970, 1980, 1990, and 2000. The simulated peak discharges at Hirakata are examined

to discuss the effect of the dams. The rainfall event used in this study is the typhoon event observed in 1982 (1-3 August). This event was chosen because it was the largest event since 1980 when enough rainfall–discharge sequences were available to conduct the simulation.

Furthermore, in order to examine which flood magnitude the dams can attenuate the peak, some factors were multiplied to the 1982 rainfall pattern. The factors are selected so that two-day total rainfall amounts in the Yodo River basin correspond to the following return periods: 30, 50, 100, 150, 200 and 300 years. The same parameters and the initial conditions used in the test simulation are used for this assessment.

(2) Results and discussion

Figure 5.7 shows the simulated peak discharge at Hirakata. The different lines represent different years. Firstly, looking at the results of 1960 when only the Setagawa weir existed, it can be observed that peak discharge caused by the 30-year return period rainfall (Q30) exceeds 12,000m^3/s, which is the allowable maximum flood discharge at Hirakata. By 1970 two other dams, the Amagase dam and the Takayama dam, had been constructed. The comparison between the lines for 1960 and 1970 indicates these two newly constructed dams successfully decrease flood peaks from relatively smaller rainfall events up to around the 50-year return period. By 1980, two more dams, the Shorenji dam and the Murou dam, had been constructed. These dams enabled the peak discharge to reduce by about 2000m^3/s compared with the discharge from the 100-year and 150-year return period rainfall. This is because the
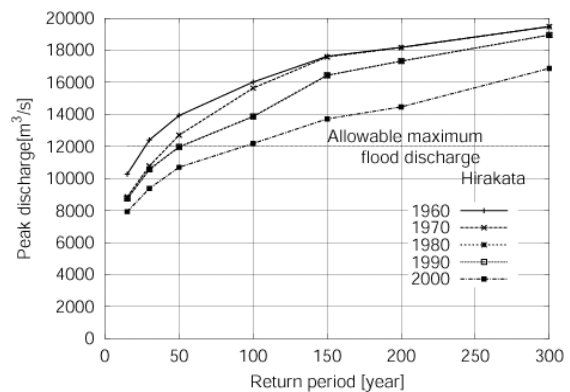

Fig. 5.7 Simulated peak discharges at Hirakata with different magnitude of input rainfall. Years (1960, 1970, etc.) denote that the dams existed in the year are included in the simulation.at Kamo
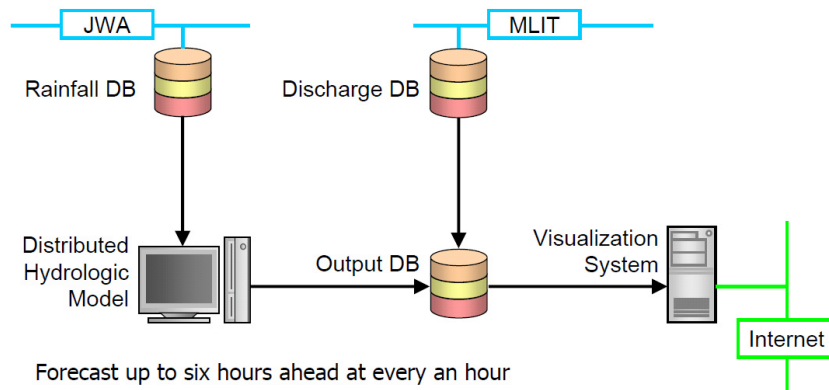
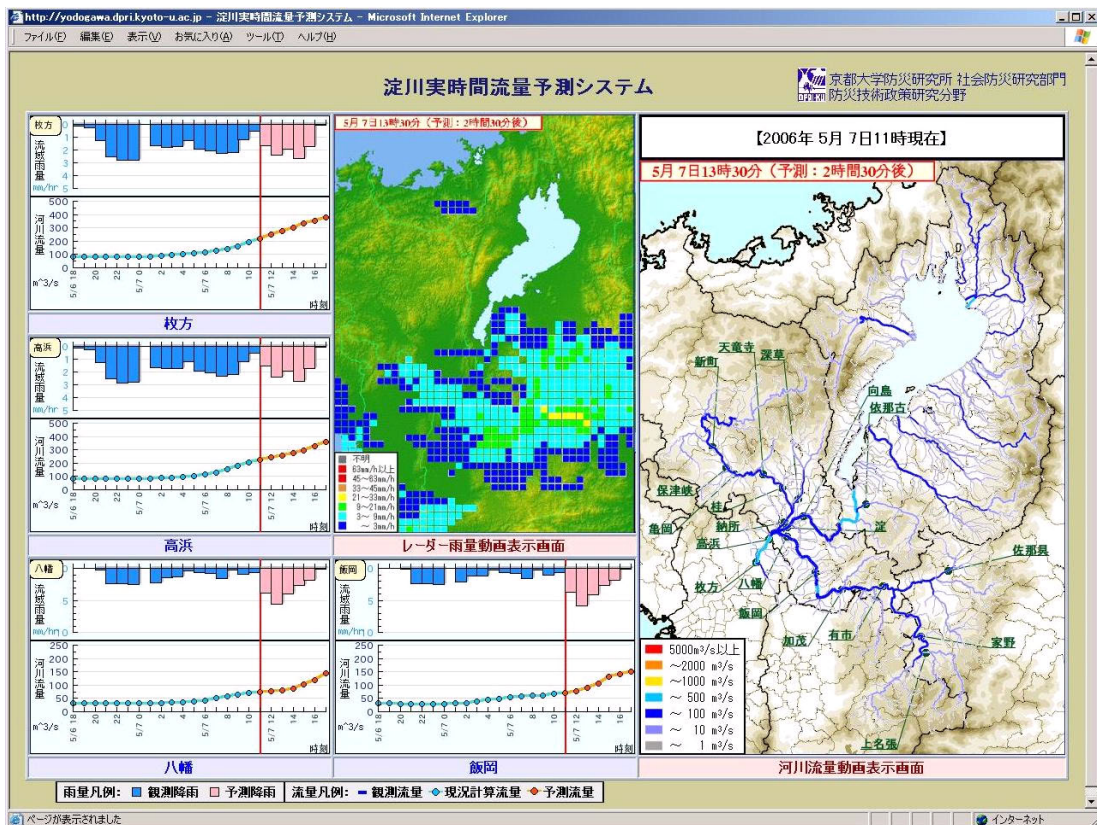Fig. 5.8 Structure of real-time flood forecasting system

Fig. 5.9 Real-time flood forecasting information system through internet

Takayama dam located at the downstream of the Shorenji dam and the Murou dam had a flood control capacity large enough to regulate floods of this magnitude. By 2000, a further three dams, the Nunome dam, the Hinachi dam, and the Hiyoshi dam, had been constructed. It is noteworthy that, in 2000, the allowable maximum flood discharge was exceeded by the discharge from the 100 year return period rainfall (Q100), whereas in 1960 this value was exceeded by the Q30 peak discharge.

5.5 Real-time flood forecasting system

The distributed rainfall-runoff system was extended for a real-time flood forecasting system which provides six-hour-ahead discharge predictions at every hour. Figure 5.8 illustrates the structure of the real-time prediction system. Rainfall predictions are provided through Japan Meteorological Agency, which is feeded into the distributed rainfall-runoff system. The prediction results are provided through internet at http://yodogawa.dpri.kyoto-u.ac.jp/ on real-time basis. Figure 5.9 is an example of the flood forecasting

information system which provides six hours ahead rainfall and discharge predictions at various points in the basins as well as the comparisons of observed and predicted rainfall and discharge in two months. The system will contribute to flood countermeasure actions especially at local governments which do not have river discharge prediction information.

5.6 Section's Conclusions

A rainfall-runoff prediction system was developed for the Yodo River basin and the system was extended for a real-time flood forecasting system. The assessments of dam effects on flood attenuation in the basin are summarized as follows:

1) The dams constructed in the 1960s were effective in attenuating relatively small flood peaks caused by the rainfall event with the magnitude of the 50-year return period or smaller. On the other hand, the dams constructed after 1970 were effective in attenuating relatively larger flood peaks caused by the rainfall events with the magnitude of the 100-year return period or larger.

2) Q30 corresponds to the allowable maximum Q30 corresponds to the allowable maximum flood discharge at Hirakata in 1960, while Q100 corresponds to it in 2000. However, we found that it has not achieved the initial design target: the discharge caused by smaller than the 200-year return period rainfall cannot exceed the allowable maximum flood discharge.

The system is extended for real-time flood prediction system, which enables to make discharge predictions for six-hours ahead at almost any river points on the Yodo River basin. The system provides flood predictions at small scale ungauged catchments in the Yodo River basin, which will help local governments to establish for flood mitigations countermeasures.

6. Concluding Remarks

The conclusions of the present research works are summarized in each section as **2.6**, **3.4**, **4.5** and **5.6**.

References

Ashida, K. and Fujita, M. (1987): Simulation of reservoir sedimentation, *Annuals of DPRI, Kyoto Univ.*, No.30 B-2 (in Japanese).

Cengel and Cimbala. (2006): Fluid mechanics, fundamental and application, McGraw-Hill International, 567p.

Fujita, M. (2004): Study on riverbed morphology as habitat for aquatic living things, *Report, River Environment Fund*, Foundation of River Watershed Environment Management (in Japanese).

Fujita, M., Tsutsumi, D., and Sulaiman, M (2005): A simulation method for quantitative and qualitative changes of riverbed, *Proc. of Int. Conf. on Fluvial and Coastal Disasters*, CD-ROM.

Hinogawa River Office of MLIT (2004): Technical Report on Integrated Sediment Management of Hino River Basin 2003 (in Japanese).

Ichikawa, Y. (2001): Framework and lumping of distributed rainfall-runoff models, *Dr. Eng. Thesis, Kyoto Univ.*, Japan (in Japanese).

Ishigaki, T., Toda, K., Baba, Y., Inoue, K., Nakagawa, H., Yoshida, Y., Taga, H. (2005): Experimental study on evacuation from underground space by using real size models, *Annuals of DPRI, Kyoto Univ.*, No.48 B, pp.639-646 (in Japanese).

Kamei, I. (1984): "Taifu ni Tsuite, Tennsai Jinnsai Sumai no Bunnkashi", *Misawa Homes Institute of Research and Development* (in Japanese).

Matsutomi, H. and Izuka, H. (1988): Tsunami current velocity on land and its simple estimation method, *Annual Jour. of Coastal Eng.*, JSCE, 45, pp.361-365.

Parker, G. (2004): 1D Sediment transport morpho-dynamics with applications to rivers and turbidity current, e-book.

Patankar, S.V. and Spalding, D.B. (1972): A calculation procedure for heat, mass and momentum transfer in three-dimensional parabolic flow, *Jour. of Heat Mass Transfer*, Vol.15, pp.1787.

Sayama, T., Tachikawa, Y., Takara, K. and Ichikawa, Y. (2005): Development of a distributed rainfall-runoff prediction system and assessment of the flood control ability of dams. *Jour. of Hydr.,Costal and Env. Eng.*, JSCE, 803 / II-73, pp.13-27 (in Japanese).

Sekine, M. and Kawakami, N. (2005): Simplified numerical model of inundation process and it's application to the urban area with underground space, *Jour. of Hydr.,Costal and Env. Eng.*, No.789/II-71, pp. 47-58 (in Japanese).

Tachikawa, Y., Nagatani, G. and Takara, K. (2004): Development of stage-discharge relationship equation incorporating saturated-unsaturated flow mechanism. *Ann. Hydraul. Eng*, JSCE, 48, pp.7-12 (in Japanese).

Tatsuzawa, H., Hayashi, H. and Hasegawa, K. (1998): Roles of heterogeneous property of bed materials for the formation of steep-pool system in mountain streams, *Annual Jour. of Hydraulic Eng.,* JSCE, Vol.42, pp.1075-1080 (in Japanese).

Toda, K., Kuriyama. K, Oyagi, R., Inoue, K. (2003): Inundation analysis of complicated underground space, *Annual Jour. of Hydraulic Eng.*, JSCE, Vol.47, pp. 877-882 (in Japanese).

Togashi, H. and. Nakamura, T. (1977): An experimental study of tsunami run-up on uniform slopes, *Coastal Eng. in Japan*, 20, pp.95-108.

Tsutsumi, D., Fujita, M., and Sulaiman, M. (2006): Changes in the void ratio and void structure of riverbed material with particle size distribution. *River, Coastal and Estuarine Morphodynamics*, Vol.2, Parker, G.,

Garcia, M.H., eds., Taylor & Francis, pp.1059-1065.

Yamamoto, D., Toda, K., Yoneyama, N. and Aihata, S. (2006): Hydraulic model test of inundation water intrusion into small scale underground space, *Proc. of River Eng.*, JSCE, Vol.12, pp.115-120 (in Japanese).

Yasuda, T., Takayama, T. and Yamamoto, H. (2006): Characteristics of deformations and forces on dispersive solitons of tsunami, *Annual Jour. of Coastal Eng.*, JSCE, 53, pp.256-260.

Yoneyama, N. and Moriya, S. (1995): Numerical analysis of 2-dimensional fluid flow with free surface using VOF technique, *Annual Jour. of Hydraulic Eng.*, No.39 (in Japanese).

Yoneyama, N. (1998): Development of free surface hydraulic analysis code (FRESH), Nagare, *Japan Society of Fluid Mech.*, Vol.17, No.3 (in Japanese).

都市水害の危険度評価技術とその社会的応用に関する研究

高山知司・寶　馨・戸田圭一・藤田正治・間瀬　肇・
立川康人・米山　望・堤　大三・安田誠宏・佐山敬洋

要　旨

　本報告は，21世紀COEプロジェクトの一研究課題である「都市水害の危険度評価技術とその社会的応用に関する研究」に係わる以下のような研究テーマに関して，2006年に行った研究の成果を概述したものである。1) 小規模地下空間への浸水過程の3次元数値解析，2) 津波避難タワーの耐津波安定性解析，3) 異なる粒径分布をもつ混合砂礫の空隙率，4) 高度制御流域における洪水予測システムとリアルタイム洪水予測への拡張。

キーワード: 3次元数値解析，浸水過程，小規模地下空間，VOFモデル，津波避難タワー，津波力，抗力係数，陸上津波流速，混合砂礫，空隙率，粒径分布，洪水予測システム，高度制御流域，リアルタイム洪水予測